Mechanistic study of an immobilised molecular electrocatalyst by in-situ gap plasmon assisted spectro-electrochemistry

Demelza Wright[1,2,6], Qianqi Lin[1,6], Dénes Berta[3,4], Tamás Földes[3,4], Andreas Wagner[2], Jack Griffiths[1], Charlie Readman[1,5], Edina Rosta[3,4*], Erwin Reisner[2*], Jeremy J. Baumberg[1*]

[1]Nanophotonics Centre, Department of Physics, Cavendish Laboratory, University of Cambridge, Cambridge, CB3 0HE, England, UK

[2]Department of Chemistry, University of Cambridge, Lensfield Road, Cambridge CB2 1EW, Cambridge, UK

[3]Department of Chemistry, King's College London, 7 Trinity Street, London SE1 1DB, UK

[4]Department of Physics and Astronomy, University College London, London WC1E 6BT, UK

[5]Melville Laboratory for Polymer Synthesis, Department of Chemistry, University of Cambridge, Lensfield Road, Cambridge CB2 1EW, UK

[6]These authors contributed equally: Demelza Wright and Qianqi Lin.

*e-mail: e.rosta@ucl.ac.uk; reisner@ch.cam.ac.uk; jjb12@cam.ac.uk

Abstract

Immobilised first-row transition metal complexes are potential low-cost electrocatalysts for selective CO_2 conversion to produce renewable fuels. Mechanistic understanding of their function is vital for the development of next-generation catalysts, though poor surface sensitivity of many techniques makes this challenging. Here, a nickel bis(terpyridine) complex is introduced as a CO_2 reduction electrocatalyst in a unique electrode geometry, sandwiched by thiol anchoring moieties between two gold surfaces. Gap-plasmon-assisted surface-enhanced Raman scattering spectroscopy coupled with density functional theory calculations reveals the nature of the anchoring group plays a pivotal role in the catalytic mechanism by eliminating ligand loss. Our *in-situ* spectro-electrochemical measurement enables the detection of as few as 8 molecules undergoing redox transformations in the individual gold-sandwiched nanocavities, together with the calibration of electrical fields *via* vibrational Stark effects. This advance allows rapid exploration of non-resonant redox reactions at the few-molecule level and provides scope for future mechanistic studies of single-molecules.

Introduction

Understanding interface organisation and charge transport between materials and molecules is a major issue plaguing the systematic development of photocatalysis, electrochemistry, and molecular electronics. An emerging tool for interfacial studies exploits plasmonic gaps constructed from metallic nanostructures,[1] which confine optical fields far below the diffraction limit to create a highly localised surface probe with enhanced spectroscopic sensitivity and selectivity. One such plasmonic gap approach is tip-enhanced Raman spectroscopy (TERS), which has been used to observe redox active molecules responding to electrochemical potential.[2,3] However, the major challenge of reliable fabrication and availability of suitable probes,[4] as well as probe degradation,[5] has precluded widespread utilisation of TERS. By contrast, although surface-enhanced Raman scattering (SERS)[6–8] at roughened surfaces is easy to implement, it is limited by poor control over surface morphologies that alter electrochemical and spectroscopic behaviours.[9] The high precision of gap-plasmon-assisted SERS (introduced below), which uses metal nanoparticles on an electrode surface, is thus becoming a valuable tool in studying real-time *in-situ* redox processes.[10]

While electron transfer at the surface of nanoparticles has been studied electrochemically,[11–13] plasmonic nano-gaps enable *in-situ* observation of both oxidised and reduced species through SERS. The high signal-to-noise ratios eliminate the need for electronically resonant enhancement, which is typically susceptible to bleaching over time. These vibrational spectroscopies serve as powerful tools to study catalysis as they provide structural fingerprint information about the catalyst. Of particular interest are immobilised systems,[14,15] where molecular catalysts are anchored to surfaces. Understanding these systems is important for designing industrially-relevant catalysts, by enhancing performance through improved electron transfer dynamics,[16,17] tuning the redox mechanisms, and improving the long-term stability of catalysts *via* facile recovery and separation from products.[18]

In this work, we perform gap-plasmon-assisted SERS coupled with electrochemistry to study the CO_2 reduction catalyst [Ni(2,2':6',2"-terpyridine-4'-thiol)$_2$](BF$_4$)$_2$ (**Ni(tpyS)$_2$**).[19] While bis(terpyridine) complexes of cobalt and nickel have been previously used for electrocatalytic CO_2 reduction,[19–21] no

56 mechanistic studies have been performed in a sandwich geometry with a highly confined volume. The

57 nickel-centred complex is chosen in this study due to its excellent selectivity for CO_2 reduction towards

58 CO over hydrogen evolution.[19–21] Using *in-situ* SERS between two gold surfaces we are able to

59 characterise the spectro-electrochemical behaviour, resolving changes in chemical bonding and

60 identifying the catalytic reaction mechanism. Comparing experimental SERS spectra with density

61 functional theory (DFT) calculations of **Ni(tpyS)₂** shows the first electron transferred during reduction

62 weakens the Au-S bonds, while the electronic environment of the metal centre changes less, confirming

63 that the nature of the anchoring group plays a pivotal role in the catalytic mechanism. Electrode design

64 such as confined environments[22] and layered geometries[23,24] advance the catalysis by enhancing

65 nanoscale mass transport and electrode dynamics compared to conventional electrodes. We utilise a

66 single-site sandwiched electrode geometry with a molecular catalyst. Compared to the conventional

67 system with solution-phase nickel catalysts,[19,20] this electrode geometry with adsorbed catalyst is likely

68 to change the reaction mechanism as it allows the gained electron from reduction to delocalise over the

69 Au-S anchoring unit, inhibits ligand loss and preserves catalyst integrity. This work gives unique

70 insights into material-molecule hybrid catalysis by going beyond prior work on redox-inactive biphenyl

71 monolayers where changes in molecule polarizability are induced electrochemically,[25] or tracking

72 resonant molecules when they enter and leave electronically-active states during redox transitions.[26]

73 **Results**

74 **Gap-plasmon-assisted spectro-electrochemical assembly.** Gap plasmon cavities have extremely

75 small mode volumes (< 50 nm^3) with high optical field enhancements (>500) that strongly amplify the

76 Raman scattering of molecules in the gap by $>10^9$. To construct the nanoparticle-on-mirror (NPoM)

77 plasmonic cavities used here, planar gold substrates are functionalised with a self-assembled monolayer

78 (SAM, see Methods). Gold nanoparticles (AuNPs) are then drop-cast on top of the monolayer (**Fig. 1a**),

79 sandwiching the active molecules in the nano-gap. The advantage of this geometry is that the gold

80 mirror conveniently forms one electrode of the cell (**Fig.1a**). Dark-field scattering spectra (**Fig. 1b,c**)

81 on each NPoM characterise the monolayer quality in the gap. These scattering spectra show transverse

82 ($\lambda_t \sim 530$ nm) and coupled ($\lambda_c \sim 700$ nm) modes in the NPoM nanocavities. The coupled plasmon at λ_c

83 arises from the interaction of the nanoparticle with its image charges in the mirror below, tightly

84 confining the plasmonic hot spot underneath the NPoM.[1,27] The position of λ_c strongly depends on the

85 properties of the gap spacer, including its thickness (d) and effective refractive index (n_g).[28] Using

86 automated tracking microscopy,[29] dark-field scattering spectra are observed for many hundreds of

87 individual NPoMs across the sample surface. Real-time spectro-electrochemical measurements are

88 achieved by incorporating NPoM samples into a 3D-printed cell. SERS spectra are recorded by

89 illuminating individual NPoMs with a continuous wave laser at wavelength $\lambda_l = 633$ nm, with

90 electrochemical potential applied simultaneously to the gold substrate using a 3-electrode configuration.

91 **Electric field calibration by vibrational Stark effect.** The electrochemical control of the applied

92 potential in the nano-gap was first probed with SERS from a calibration molecule, PDI (1,4-phenylene

93 diisocyanide) (**Fig. 1a**). Scattering spectra for PDI monolayers are measured from automated tracking

94 of >400 NPoMs (**Fig. 1b**). These give near-identical coupled modes at $\lambda_c = 739 \pm 22$ nm (**Fig. 1c**),

95 indicating a highly consistent monolayer over the gold substrate (standard error matches variation in

96 nanoparticle size and shape[30]). Modelling the coupled mode resonance[28] gives $n_{g,\mathrm{PDI}} = 1.4$ and $d_{\mathrm{PDI}} =$

97 1 nm, which is consistent with the thickness expected for a monolayer in which the molecules bind to

98 the substrate in a near-vertical rather than flat orientation. SERS spectra for PDI in NPoMs (**Fig. 1d**)

99 are recorded at potentials ranging from −0.6 to +0.2 V (*vs.* Ag/AgCl) in a N_2-saturated aqueous solution

100 with a 0.1 M KCl supporting electrolyte. In this electrochemically inert range for PDI (Supplementary

101 **Fig. 1**), the SERS band near 2130 cm^{-1} shows a significant blue-shift as positive potential is applied,

102 shifting linearly at 30 ± 4 cm^{-1} V^{-1} (**Fig. 1e**, black). This is consistent with the stretching mode for

103 isocyanide (N≡C) bound to the gold surface[31]. For comparison, SERS spectra for PDI at

104 electrochemically roughened gold surfaces are recorded and analysed (**Fig. 1e**, grey) in the same

105 conditions, where v(N≡C) shifts by 31 ± 1 cm^{-1} V^{-1}.
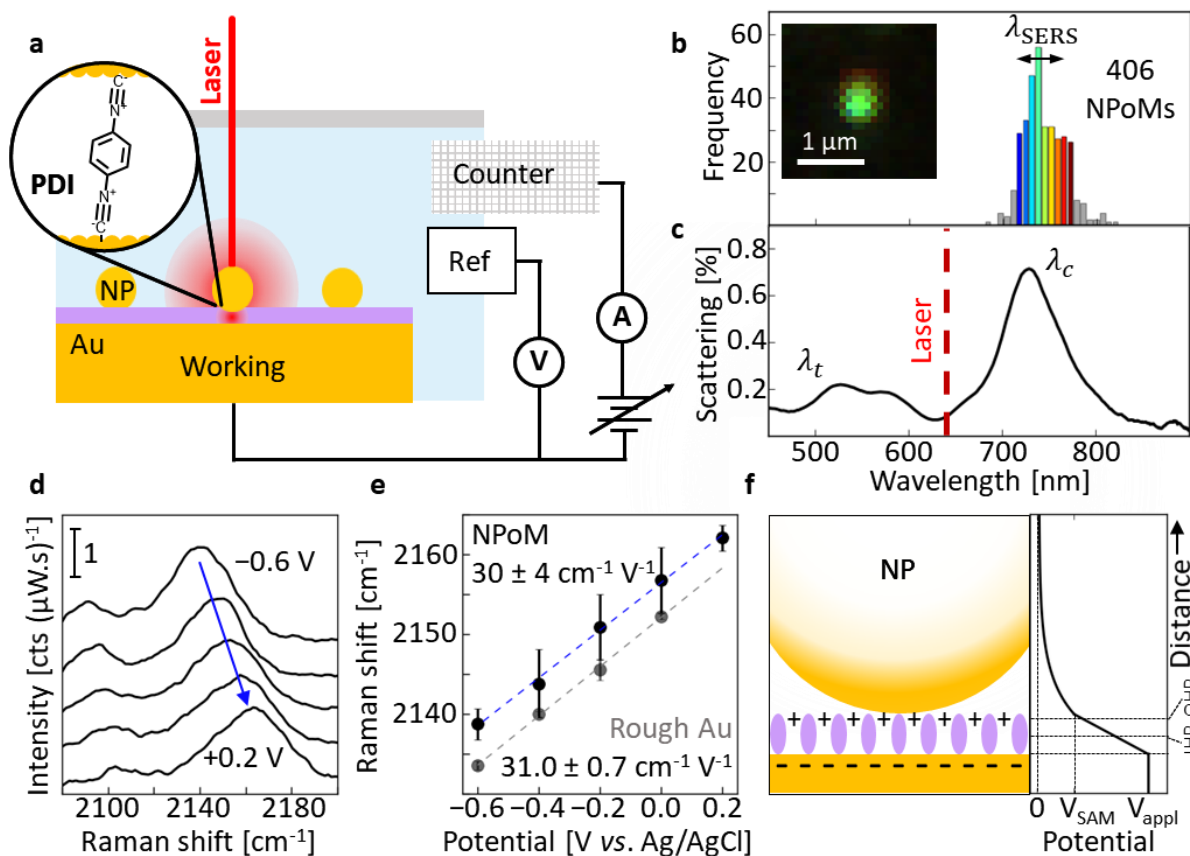
Fig. 1 | Electric field calibration in nanoparticle-on-mirror (NPoM). a, NPoM geometry in spectro-electrochemical cell using three electrodes: gold mirror working electrode, platinum counter electrode and 3 M KCl Ag/AgCl reference electrode. Inset: PDI molecule. **b**, Histogram of plasmon coupled mode positions. Inset shows spatial dark field image of single 80 nm diameter NPoM. **c**, Dark-field scattering spectra for PDI monolayer in NPoM. **d**, SERS spectra for PDI in gold nano-gap in aqueous solution with 0.1 M KCl and saturated with N_2, showing $\nu(N\equiv C)$ region at different bias. **e**, Potential-dependent $\nu(N\equiv C)$. Black: NPoMs, grey: roughened gold surface. Error bars refer to standard deviation, $n = 50$ measurements for NPoM, $n = 80$ measurements for roughened gold. **f**, Model of electrical double layer in NPoM and potential drop across the gap.

These SERS shifts arise from the vibrational Stark effect (VSE),[31–33] where the vibrational energies of chemical bonds are perturbed by an electric field. The Stark shift versus potential, known as the Stark tuning rate, enables direct measurement of the potential gradient at the electrode. Our measurements provide direct evidence that the electrochemical potential gradient (*i.e.* electric field) at the NPoM surface of a SAM is identical to that found at a roughened electrode surface of a SAM. While electron tunnelling has been reported across NPoM plasmonic gaps, the electron transfer process at the interface between the SAM and this sandwiched electrode geometry remains unclear.[12,13] To address this question, a model of the electrical double layer[31,34] for the NPoM junction (**Fig. 1f**) is developed here. As the SAM is adsorbed on the gold substrate, the electrical centre of the monolayer is the Inner Helmholtz Plane (IHP). Solvated ions from the supporting electrolyte approach the SAM by diffusion,

124 and the position of these nearest ions is the Outer Helmholtz Plane (OHP), roughly corresponding to

125 the length of molecules ($d = 1$ nm). Following the double layer capacitive (non-Faradaic) charging, the

126 potential drops rapidly within the OHP. Faradaic electron transfer takes place readily between the gold

127 substrate and the monolayer (as observed below). This electron transfer process is similar to the case

128 when no nanoparticle is on top of the SAM, implying that electron tunnelling is not the only path across

129 the gaps, otherwise the VSE should not be observed. In fact, the electron tunnelling is less efficient due

130 to the 1 nm barrier width[35] and hence an electron transfer process through the SAM dominates

131 (Supplementary **Fig. 2**).

132
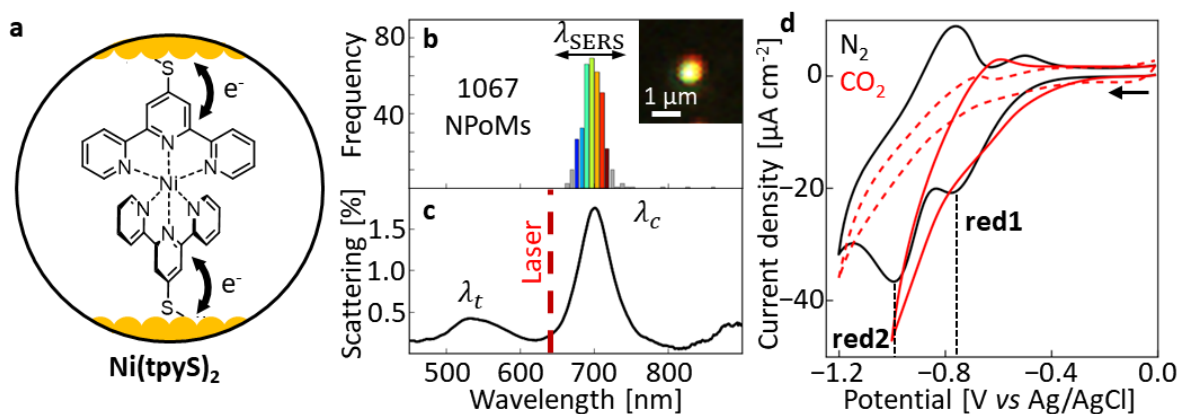
Fig. 2 | Dark-field scattering spectroscopy and electrochemistry for Ni(tpyS)₂. a, **Ni(tpyS)₂** in nanoparticle-on-mirror
(NPoM) geometry. **b**, Histogram of plasmon coupled mode positions. Inset shows spatial image of single 60 nm diameter
NPoM. **c**, Scattering spectra for **Ni(tpyS)₂** monolayer in NPoM. **d**, Cyclic voltammograms for NPoMs with (solid lines) or
without (dashed line) **Ni(tpyS)₂** monolayer in pH 3.8 aqueous solution supported with 0.1 M KCl and saturated with N_2 (black)
or CO_2 (red). Scan rate = 100 mV s⁻¹.

Spectro-electrochemical studies of immobilised Ni(tpyS)₂. Using **Ni(tpyS)₂** in the nano-gap (**Fig. 2a**)

139 allows tracking of redox and catalytic reactions. Scattering spectra for **Ni(tpyS)₂** monolayer measured

140 from >1000 NPoMs (**Figs. 2b,c**) shows the coupled mode at $\lambda_c = 696 \pm 15$ nm, confirming the

141 monolayer is uniform with $n_{g,\mathbf{Ni(tpyS)_2}} = 1.4$ and $d_{\mathbf{Ni(tpyS)_2}} = 1.5$ nm. A dark field image (Supplementary

142 **Fig. 3**) demonstrates nanoparticle distribution. Cyclic voltammetry (CV) for **Ni(tpyS)₂** NPoMs is first

143 recorded in a N_2-saturated pH 3.8 aqueous solution supported with 0.1 M KCl, from 0 to -1.2 V (*vs*

144 Ag/AgCl) and back to 0 V (**Fig. 2d**, black). Two reductive waves are observed: **red1** at $E_p = -0.76$ V

145 and **red2** at $E_p = -0.99$ V, corresponding to the first and second reduction of **Ni(tpyS)₂**.[19,20] These

146 electrochemical responses are markedly different from the voltammogram when no nanoparticle is on

147 top of the Au-**Ni(tpyS)₂** monolayer (Supplementary **Fig. 4**, blue). In the absence of AuNPs, the lack of

148 oxidative waves indicates the redox process is chemically irreversible. This may in part be due to the

149 loss of one tpyS ligand. While in the NPoM construct, the presence of two oxidative waves supports a

150 chemically reversible process, confirming preservation of the tpyS ligand coordinated to the nickel

151 centre. Voltammetric features of **Ni(tpyS)₂** are significantly clearer, indicating that the voltammogram

152 is dominated by the molecules underneath the nanoparticles, rather than the exposed monolayer. As a

153 result, the CV directly measures conditions in the gap. More importantly, while a broad peak at −0.86

154 V is observed in the absence of the nanoparticle on top (Supplementary **Fig. 4**, blue), the presence of

155 nanoparticles shows a well-defined reductive peak shifting by ~+0.1 V (Supplementary **Fig. 4**, black).

156 This can be explained by the reduction of the monolayer becoming thermodynamically more

157 favourable, due to stabilisation of the reduced radical species *via* adsorption by the nanoparticle on top

158 (Supplementary **Fig. 4d**).[36] The nanoparticle further stabilises the adsorbed system by withdrawing

159 electron density from the monolayer, making reduction easier. This stabilisation is not molecule

160 specific, as for PDI the $v(N{\equiv}C)$ shifts by ~−5 cm^{-1} in NPoMs *vs.* a rough gold electrode (**Fig. 1e**). NPoM

161 plasmonic cavities thus significantly enhance interfacial electron transfer.

162 The CV for CO_2 catalytic reduction is recorded in a CO_2-saturated solution with **Ni(tpyS)₂** NPoMs (**Fig.**

163 **2d**, red solid line), and compared with CO_2 reduction on the gold substrate without **Ni(tpyS)₂** monolayer

164 in the same solution (**Fig. 2d**, red dashed line). Comparison of these shows over 2-fold increased current

165 density with the onset potential shifting to ~−0.52 V, illustrating that the electrocatalytic CO_2 reduction

166 is mediated by **Ni(tpyS)₂** NPoMs before proton reduction on gold.[25]
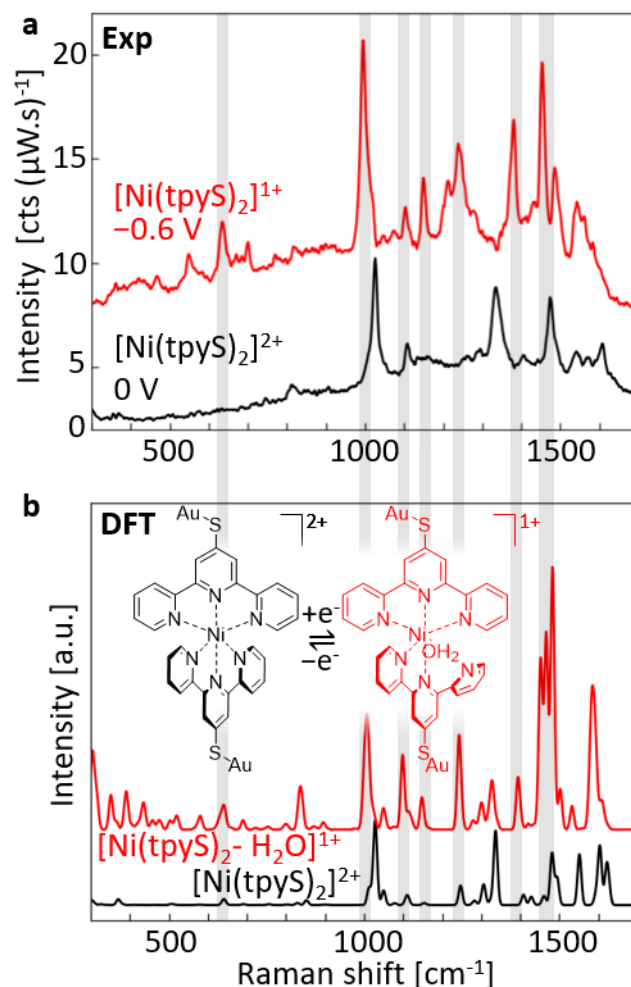
Fig. 3 | Surface-enhanced Raman spectroscopy (SERS) and density functional theory (DFT) calculations for Ni(tpyS)₂.
a, Experimental SERS spectra of **Ni(tpyS)₂** in nanoparticle-on-mirror (NPoM) at 0 V (black) and −0.6 V (red, difference spectrum) *vs* Ag/AgCl in pH 3.8 aqueous solution supported with 0.1 M KCl and saturated with N_2. Additional bands appearing at −0.6 V are highlighted in grey. **b**, DFT calculations for $[Ni(tpyS)_2]^{2+}$ and $[Ni(tpyS)_2\text{-}H_2O]^{1+}$.

SERS is now used to explore chemical bonding changes. SERS spectra (**Fig. 3a**) are recorded for the reduced state ($[Ni(tpyS)_2]^{1+}$, −0.6 V) and oxidised state ($[Ni(tpyS)_2]^{2+}$, 0 V *vs.* Ag/AgCl, according to the CV in **Fig. 2d**). To avoid proton reduction[25] which forms bubbles disrupting the optical measurements, potentials are kept at −0.6 V to observe **Ni(tpyS)₂** in the first reduced state only. Comparison of these spectra shows that during reduction, the SERS background increases and several spectral bands emerge (highlighted in grey). Despite attenuation and scattering from the spectro-electrochemical cell, SERS signals exceed 10 cts $(\mu W.s)^{-1}$ with a high signal-to-noise ratio. While **Ni(tpyS)₂** is electronically non-resonant at $\lambda_l = 633$ nm (Supplementary **Fig. 5** shows no absorption/emission at λ_l, which is essential to correctly measure electrochemical performance), the

181   near-resonant plasmonic mode at 696 nm strongly enhances the SERS (**Fig. 2c**). Similar measurements

182   for **Ni(tpyS)₂** on an electrochemically roughened gold substrate (Supplementary **Fig. 6**) show spectral

183   changes in the reduced $[Ni(tpyS)_2]^{1+}$ state, though with broader, less defined SERS bands with an

184   order of magnitude lower intensity.

185   DFT calculations are performed to simulate the SERS responses for **Ni(tpyS)₂** in different redox states.

186   Comparison of computational spectra with experimental SERS for $[Ni(tpyS)_2]^{2+}$ (black lines **Figs.**

187   **3a,b**) shows excellent agreement. We consider several possible reduction products for bis(terpyridine)

188   complexes involving different mechanisms including those in refs. [19,21]. The calculated Raman spectra

189   (Supplementary **Fig. 7**) shows that $[Ni(tpyS)_2\text{-}H_2O]^{1+}$ involving a one electron reduction of the ligand

190   and an addition of a water molecule to the nickel coordination gives the best agreement with

191   experiments (red lines in **Fig. 3**). The spectral bands are labelled with relevant vibrational modes and

192   discussed in Supplementary **Fig. 8** and Supplementary Note 1**.** Further DFT calculations considering

193   effects of the electrical double layer on the polarization of dipoles (Supplementary **Fig. 9**) shows the

194   same spectral matching results with calculations from isotropic and unpolarized environments. The first

195   reduction process **red1** (**Fig. 2d**) is thus identified as the electron transfer step:

$$[Ni(tpyS)_2]^{2+}(ads) + e^- + H_2O(aq) \rightleftharpoons [Ni(tpyS)_2\text{-}H_2O]^{1+}(ads) \qquad (1)$$
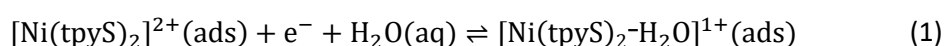
196   The reduction process for the dissolved non-thiolated catalyst, [Ni(2,2':6',2"-terpyridine)₂](BF₄)₂

197   (**Ni(tpy)₂**), has been suggested to accompany the loss of one terpyridine ligand to form an active

198   mono(terpyridine) complex.[19] With the unique sandwiched electrode geometry and thiolated catalyst

199   here, mono(terpyridine)-nickel complex was not observed in our spectra (Supplementary **Fig. 7**).

200   Instead, the calculated charge distribution shows the single electron gained from reduction is not

201   localised at the metal centre and instead perturbs the Au-S bond (Supplementary **Fig. 10**). This is

202   consistent with the reported electrochemistry for the nickel-centred bis(terpyridine) complexes, where

203   ligand-based redox dominates[20] due to the relative stability of Ni^{2+} d^8 outer shell electron configuration.
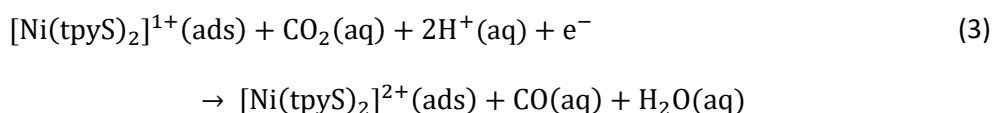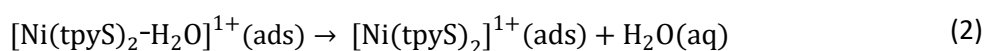
204 In addition to weakening the Au-S bond, DFT also shows that bond orders for the coordination bonds

205 are affected (Supplementary **Table 1**). The axial Ni-N bonds on both tpyS ligands are strengthened, but

206 the equatorial Ni-N bonds are weakened during reduction. Since partial ligand exchange is

207 thermodynamically favourable when the complex is reduced, solvent access to the nickel centre for

208 coordination is proposed. This is confirmed by comparison of calculated and experimental spectra of

209 the reduced state by a discrete implementation of the earth mover's algorithm (Supplementary Note 2),

210 whereby we find a significant improvement in spectral agreement when including a coordinated water

211 molecule (Supplementary **Fig. 7**). Since the complexes are octahedral, at least one of the existing

212 coordination bonds must be broken to allow CO_2 binding to the metal centre for subsequent catalytic

213 reduction. Our experiments and computations strongly support this reaction is realised through the

214 breaking of a single Ni-N bond followed by rotation of a pyridine unit from one tpyS ligand.

215 (Supplementary **Fig. 7**).
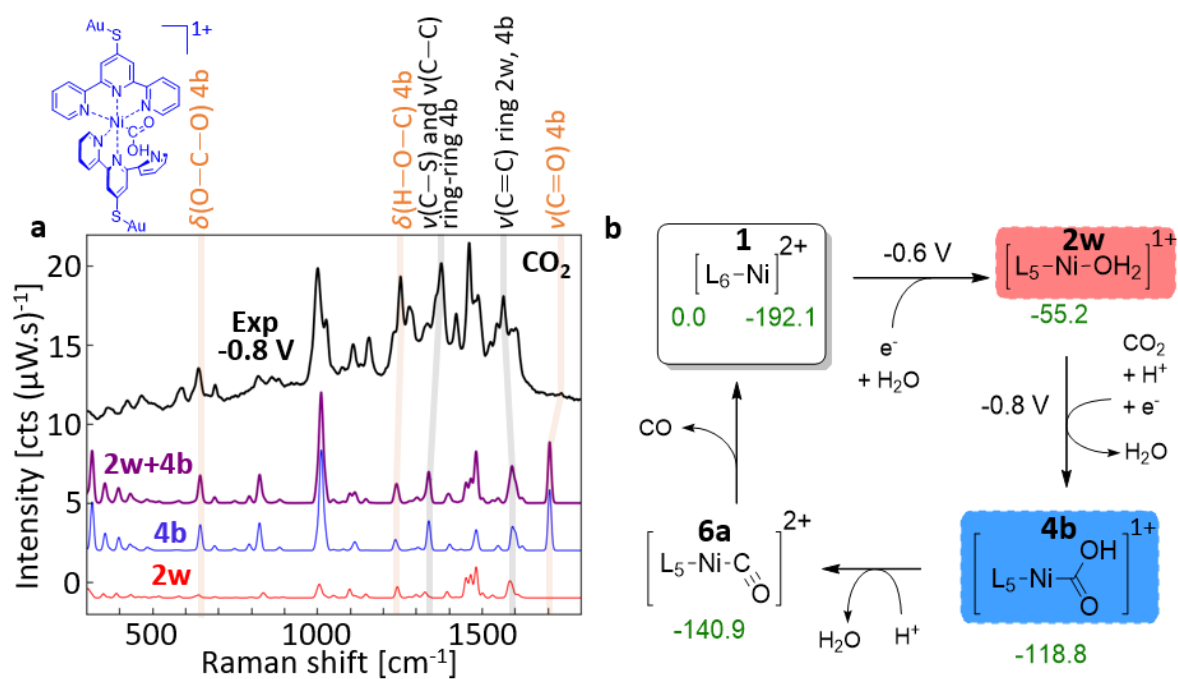
216

217 **Fig. 4 | Ni(tpyS)₂ catalysed CO₂ reduction. a**, Experimental SERS of **Ni(tpyS)₂** averaged from different nanoparticle-on-
218 mirror (NPoM)s in CO₂-saturated pH 3.8 aqueous solution at −0.8 V and DFT calculated best-matched purple spectrum. The
219 latter is from linear combination of the red and blue spectra, corresponding to their colour-shaded intermediates respectively
220 in **b**. Grey bars highlight matching spectral bands between experiments and calculations. Vibrational modes relevant to CO₂
221 reduction are highlighted in orange. More vibrational modes are shown in Supplementary **Figs. 8** and **15**. **b**, Proposed catalytic
222 cycle of **Ni(tpyS)₂** mediated CO₂ reduction. Relative Gibbs free energies (kcal mol⁻¹) are displayed in green. Shaded
223 intermediates are spectroscopically verified. L_n represents tpyS ligands forming n Ni-N bonds. $[L_6\text{-Ni}]^{2+} = [\text{Ni(tpyS)}_2]^{2+}$, [L₅-
224 Ni-H₂O]¹⁺ = [Ni(tpyS)₂-H₂O]¹⁺.

Mechanistic studies of Ni(tpyS)$_2$ mediated CO$_2$ reduction. Performing SERS in the presence of CO$_2$, several new spectral modes emerge (**Fig. 4a**, black). Gibbs energies (Supplementary **Table 3** and Supplementary **Fig. 11**) and Raman spectra (Supplementary **Fig. 12**) were calculated for 22 different reaction intermediates (Supplementary Note 2, Supplementary Table 2). Experimental SERS measurements were compared with DFT calculated single and combined spectra obtained as a mixture of two or three intermediates (Supplementary **Fig. 13** and Supplementary **Table 4**). In calculations, the effect of electron transfer was estimated based on the measured half-cell potentials. The catalytic 2H$^+$/2e$^-$ reduction of CO$_2$ overall is:

$$[Ni(tpyS)_2\text{-}H_2O]^{1+}(ads) \rightarrow [Ni(tpyS)_2]^{1+}(ads) + H_2O(aq) \tag{2}$$

$$[Ni(tpyS)_2]^{1+}(ads) + CO_2(aq) + 2H^+(aq) + e^- \tag{3}$$
$$\rightarrow [Ni(tpyS)_2]^{2+}(ads) + CO(aq) + H_2O(aq)$$

Where eq. (2) illustrates the creation of a vacant site on $[Ni(tpyS)_2]^{1+}$ as H$_2$O dissociates. We have explored the possible intermediates for a different order of electron and proton transfer steps (Supplementary **Table 2**). Only spectra from the most feasible structures according to calculated Gibbs and electronic energies were used for spectral matches (Supplementary **Fig. 12**). Deprotonated carboxyl groups bound to the nickel centre have been reported as intermediates in bis(terpyridine) complexes catalysing CO$_2$ reduction.[19,37] We performed geometry optimizations for structures where we removed the proton covalently bonded to the CO$_2$ (Supplementary **Fig. 14**). Most of these calculations show CO$_2$ detachment from the complex. For the only successfully converged structure, the reaction relative free energy for deprotonation was calculated as +10 kcal mol^{-1}, hence the intermediate is less stable when deprotonated. This free energy can be interpreted as a pK_a of 7.3 while the experiments are performed at pH 3.8, confirming the carboxyl group is protonated. Further calculations find pK_a of the pendant pyridyl group as −9.3 for $[Ni(tpyS)_2\text{-}H_2O]^{1+}$, which is not equivalent to the free unsubstituted ligand in solution[38] (see Supplementary **Table 5**, Supplementary Note 4). Despite the similarity of the molecules to those in the literature, bis(terpyridine) ligands have been used as homogeneous systems where a

247 terpyridine has been proposed to dissociate after its first reduction. Our work is performed in a confined

248 environment with two Au-S anchoring points imposing electronic and steric constraints on the system,

249 giving distinctive pK_a and intermediates.

250 The best spectral match in CO_2 conditions (**Fig. 4a**, purple) is a linear combination of two different

251 species (**Fig. 4a**, red and blue) that correspond to the shaded intermediates in **Fig. 4b**. Vibrational modes

252 of these intermediates are assigned and discussed in Supplementary Note 5 and Supplementary **Figs. 8**

253 and **15**. v(C=O) is low intensity and absent from some NPoMs, due to weak enhancement when C=O

254 is near perpendicular to the gap optical field (in the DFT unpolarized excitations are used). We find

255 (Supplementary **Table 4**) 75% of the spectral contribution is from $[L_5\text{-Ni-OH}_2]^{1+}$ (see full structure in

256 **Fig. 3b**, red), and 25% is from $[L_5\text{-Ni-COOH}]^{1+}$ (see full structure in **Fig. 4a**, blue). Using the size of

257 individual nanostructures and single molecules, the number of molecules in the plasmonic hotspot can

258 be estimated geometrically as 32 (see Supplementary Note 6). Combining these numbers, we are able

259 to detect and identify ~8 molecules undergoing catalytic turnover optically. Consecutive SERS spectra

260 with real-time chronoamperometry (Supplementary **Fig. 6**) show more stochastic behaviour of

261 reduction onset for NPoM samples compared with electrochemically roughened gold, as is expected for

262 the few-molecule regime.

263 A catalytic cycle is proposed (**Fig. 4b**) based on combined spectroscopic and computational results.

264 Following the initial reduction and Ni-N bond breaking, the water coordinated species $[L_5\text{-Ni-OH}_2]^{1+}$

265 is formed. The water molecule is highly labile and creates a vacant site on the nickel centre as it

266 dissociates. After the second reduction step, the nickel centre is sufficiently nucleophilic to attack the

267 CO_2 carbon atom, forming CO as the catalytic product. **Fig. 16** and Supplementary Note 7 contain

268 further discussion.

269 **Conclusions**

270 We have introduced a electrode geometry for *in-situ* spectro-electrochemical SERS measurement with

271 excellent signal-to-noise ratios owing to gap-plasmon enhancements. We spectroscopically track the

redox transitions of as few as 8 molecules, showing that single molecular catalyst spectroscopy is within reach. The electrochemical properties of the nanoparticle-on-mirror (NPoM) electrode are compared with the standard roughened gold electrode *via* the vibrational Stark effect, finding that NPoM is a promising electrode geometry for surface bound species. Utilising this electrode, we probe the electrocatalytic mechanism of CO_2 reduction by the molecular catalyst, **Ni(tpyS)$_2$**. Through virtual screening of intermediates in combination with SERS, we identify a reaction pathway that involves an anchoring group-based intermediate species, emphasising that the nature of the anchoring group can play a pivotal role for surface-bound catalysis. This electrode geometry successfully tunes the catalytic reaction mechanism by preventing ligand loss and hence facilitates facile recovery of catalyst.

Methods

Assembly of Ni(tpyS)$_2$. All chemicals were purchased from Sigma-Aldrich unless stated otherwise, at the highest purity available and used as received. **Ni(tpyS)$_2$** is the abbreviation for [Ni(2,2':6',2"-terpyridine-4'-thiol)$_2$](BF$_4$)$_2$. It was assembled by a previously reported procedure.[19] 2,2':6',2"-terpyridine-4'-thiol (tpyS) was purchased from HetCat (Switzerland) and Ni(BF$_4$)$_2$.6H$_2$O was purchased from Acros Organics.

Electrode preparation. Gold electrodes were fabricated by the template-stripping method as reported elsewhere[39]. **Ni(tpyS)$_2$** SAMs were formed by immersing gold electrodes in a 1 mM **Ni(tpyS)$_2$** acetonitrile solution for 22 hours, rinsing with acetonitrile and drying with compressed N$_2$. Standard gold nanoparticles (AuNPs) in a citrate buffer were purchased from BBI solutions[30] (60 nm, 80 nm) with reported morphology[10]. AuNPs were deposited by drop-casting AuNP solution onto the sample for 20 s, rinsing with distilled water and drying with compressed N$_2$. Electrochemically roughened gold electrodes were made using an established oxidation and reduction cycling method[40]. Gold films were immersed in 0.1 M KCl and potentiostatted at -0.6 V *vs* Ag/AgCl for 10 s, then swept to 1.1 V and held at this potential for 2 s. The samples were swept back to -0.6 V and these steps were repeated 25 times. **Ni(tpyS)$_2$** monolayer was formed as above.

Spectro-electrochemical cell. A specially designed three-electrode 3D-printed cell is used for all spectro-electrochemical measurements. NPoM samples are used as working electrode, a platinum mesh (Alfa Aesar) as counter electrode, and Ag/AgCl (3 M KCl, eDAQ ET072, Green Leaf Scientific) as reference electrode. The cell is closed by a $25 \times 25 \times 0.2$ mm glass cover slip. Sample to coverslip distance is approximately 0.3 mm to allow high NA collection of SERS scattering. Electrochemical measurements were recorded on a CompactStat (Ivium Technologies) or an Autolab PGSTAT204 (Metrohm).

SERS collection. SERS measurements were recorded on a modified Olympus BX51 coupled to a 633 nm laser set at powers below 100 μW. Excitation and collection were through an Olympus MPLFLN100xBD NA0.9 objective. Spectra were recorded by an Andor camera coupled to a Triax 320 spectrometer.

Dark-field scattering spectroscopy. Dark field spectroscopy was performed on a modified Olympus BX51 coupled to an incoherent white light source. Excitation and collection were through a 0.8 NA Olympus LWD BF/DF objective. Spectra were recorded on a fibre-coupled OceanOptics QE65000. Automated scans were performed by a Python particle tracking code.[29] A standard diffuser was used as a reference to normalise white light scattering.

UV/Vis collection. UV-Vis spectra were recorded on a Cary 50 (Varian) with a quartz UV-Visible cuvette (Fisher).

DFT calculations. Absorbed **Ni(tpyS)$_2$** molecules were modelled as thiol groups anchored to single gold atoms on both ends. DFT from a single Au atom shows an excellent match with the experimental SERS[41] at a much lower computational cost comparing to DFT from large Au clusters,[17,31] and is sufficient to describe any charge transfer to the molecules. Although Ni(II) can form square planar and tetrahedral complexes, bis(terpyridine) ligands form strong octahedral coordination due to steric considerations.[42] DFT optimization performed for $[Ni(tpyS)_2]^{2+}$ gives a clear preference for the tetrahedral rather than square planar by a relative free energy of -24.4 kcal mol^{-1}. Both literature and

322 DFT optimization thus confirm this geometry. Geometry optimizations and frequency calculations were

323 performed with B3LYP[43] hybrid functional and def2SVP basis set including core potentials as

324 implemented in Gaussian09 Revision E.[44] Non-covalent interactions were corrected using Grimme's

325 dispersion correction version 3 with Becke-Johnson dumping.[45] Charge distribution and bond indices

326 were calculated using the natural bond analysis (NBO) package.[46,47] Free energies were estimated based

327 on single point electronic energies calculated with def2TZVPP[48] basis set, thermal corrections obtained

328 using RRHO approximation, solvent correction was incorporated with PCM solvation using SMD

329 parametrisation.[49] Stability of the wave functions were ensured in all cases. Free energy corrections

330 were introduced for both reduction steps as $\Delta G = eV$, cost of protonation was calculated for the pH of

331 3.8 based on the experimental free energy of a solvated proton.[50] Computational spectra were scaled by

332 a factor of 0.978 to match with experiment. More details on the matching are available in Supplementary

333 Note 2.

Data availability

335 The data that support the findings of this study are available from the University of Cambridge data

336 repository at DOI: 10.17863/CAM.60379.

Code availability

338 The code for automated dark field spectroscopy measurement is available at the nplab Github

339 repository: https://github.com/nanophotonics/nplab.

340

References

1. Baumberg, J. J., Aizpurua, J., Mikkelsen, M. H. & Smith, D. R. Extreme nanophotonics from ultrathin metallic gaps. *Nat. Mater.* **18**, 668 (2019).

2. Pfisterer, J. H. K. & Domke, K. F. Unfolding the versatile potential of EC-TERS for electrocatalysis. *Curr. Opin. Electrochem.* **8**, 96–102 (2018).

3. Kang, G., Yang, M., Mattei, M. S., Schatz, G. C. & Van Duyne, R. P. *In Situ* Nanoscale Redox Mapping Using Tip-Enhanced Raman Spectroscopy. *Nano Lett.* **19**, 2106–2113 (2019).

4. Schmid, T., Opilik, L., Blum, C. & Zenobi, R. Nanoscale Chemical Imaging Using Tip-Enhanced Raman Spectroscopy: A Critical Review. *Angew. Chemie Int. Ed.* **52**, 5940–5954 (2013).

5. Kumar, N. *et al.* Extending the plasmonic lifetime of tip-enhanced Raman spectroscopy probes. *Phys. Chem. Chem. Phys.* **18**, 13710–13716 (2016).

6. Wu, D.-Y., Li, J.-F., Ren, B. & Tian, Z.-Q. Electrochemical surface-enhanced Raman spectroscopy of nanostructures. *Chem. Soc. Rev.* **37**, 1025–1041 (2008).

7. Zong, C., Chen, C. J., Zhang, M., Wu, D. Y. & Ren, B. Transient Electrochemical Surface-Enhanced Raman Spectroscopy: A Millisecond Time-Resolved Study of an Electrochemical Redox Process. *J. Am. Chem. Soc.* **137**, 11768–11774 (2015).

8. Wain, A. J. & O'Connell, M. A. Advances in surface-enhanced vibrational spectroscopy at electrochemical interfaces. *Adv. Phys. X* **2**, 188–209 (2017).

9. Willets, K. A. & Van Duyne, R. P. Localized Surface Plasmon Resonance Spectroscopy and Sensing. *Annu. Rev. Phys. Chem.* **58**, 267–297 (2007).

10. Benz, F. *et al.* SERS of Individual Nanoparticles on a Mirror: Size Does Matter, but so Does Shape. *J. Phys. Chem. Lett.* **7**, 2264–2269 (2016).

11. Chazalviel, J.-N. & Allongue, P. On the Origin of the Efficient Nanoparticle Mediated Electron Transfer across a Self-Assembled Monolayer. *J. Am. Chem. Soc.* **133**, 762–764 (2011).

12. Zhao, J., Bradbury, C. R. & Fermín, D. J. Long-Range Electronic Communication between Metal Nanoparticles and Electrode Surfaces Separated by Polyelectrolyte Multilayer Films. *J. Phys. Chem. C* **112**, 6832–6841 (2008).

13. Shein, J. B., Lai, L. M. H., Eggers, P. K., Paddon-Row, M. N. & Gooding, J. J. Formation of Efficient Electron Transfer Pathways by Adsorbing Gold Nanoparticles to Self-Assembled Monolayer Modified Electrodes. *Langmuir* **25**, 11121–11128 (2009).

14. Wang, L., Polyansky, D. E. & Concepcion, J. J. Self-Assembled Bilayers as an Anchoring Strategy: Catalysts, Chromophores, and Chromophore-Catalyst Assemblies. *J. Am. Chem. Soc.* **141**, 8020–8024 (2019).

15. Dalle, K. E. *et al.* Electro- and Solar-Driven Fuel Synthesis with First Row Transition Metal Complexes. *Chem. Rev.* **119**, 2752–2875 (2019).

16. Materna, K. L., Crabtree, R. H. & Brudvig, G. W. Anchoring groups for photocatalytic water oxidation on metal oxide surfaces. *Chem. Soc. Rev.* **46**, 6099–6110 (2017).

17. Clark, M. L. *et al.* CO2 Reduction Catalysts on Gold Electrode Surfaces Influenced by Large Electric Fields. *J. Am. Chem. Soc.* **140**, 17643–17655 (2018).

18. Cunillera, A. *et al.* Highly Efficient Rh-catalysts Immobilised by π-π Stacking for the

Asymmetric Hydroformylation of Norbornene under Continuous Flow Conditions. *ChemCatChem* **11**, 2195–2205 (2019).

19. Kuehnel, M. F., Orchard, K. L., Dalle, K. E. & Reisner, E. Selective Photocatalytic CO_2 Reduction in Water through Anchoring of a Molecular Ni Catalyst on CdS Nanocrystals. *J. Am. Chem. Soc.* **139**, 7217–7223 (2017).

20. Elgrishi, N., Chambers, M. B., Artero, V. & Fontecave, M. Terpyridine complexes of first row transition metals and electrochemical reduction of CO_2 to CO. *Phys. Chem. Chem. Phys.* **16**, 13635–13644 (2014).

21. Leung, J. J. *et al.* Solar-driven reduction of aqueous CO_2 with a cobalt bis(terpyridine)-based photocathode. *Nat. Catal.* **2**, 354–365 (2019).

22. Bae, J. H., Han, J.-H. & Chung, T. D. Electrochemistry at nanoporous interfaces: new opportunity for electrocatalysis. *Phys. Chem. Chem. Phys.* **14**, 448–463 (2012).

23. Ai, L., Tian, T. & Jiang, J. Ultrathin Graphene Layers Encapsulating Nickel Nanoparticles Derived Metal–Organic Frameworks for Highly Efficient Electrocatalytic Hydrogen and Oxygen Evolution Reactions. *ACS Sustain. Chem. Eng.* **5**, 4771–4777 (2017).

24. Yang, Y., Liu, Z. & Lian, T. Bulk Transport and Interfacial Transfer Dynamics of Photogenerated Carriers in CdSe Quantum Dot Solid Electrodes. *Nano Lett.* **13**, 3678–3683 (2013).

25. Di Martino, G. *et al.* Tracking Nanoelectrochemistry Using Individual Plasmonic Nanocavities. *Nano Lett.* **17**, 4840–4845 (2017).

26. Jiang, S. *et al.* Investigation of Cobalt Phthalocyanine at the Solid/Liquid Interface by Electrochemical Tip-Enhanced Raman Spectroscopy. *J. Phys. Chem. C* **123**, 9852–9859 (2019).

27. Olalla, P. Optical transport and sensing in plexcitonic nanocavities. *Opt. Express* **21**, 2649–2654 (2013).

28. Benz, F. *et al.* Generalized Circuit Model for Coupled Plasmonic Systems. *Opt. Express* **23**, 33255–33269 (2015).

29. De Nijs, B. *et al.* Unfolding the contents of sub-nm plasmonic gaps using normalising plasmon resonance spectroscopy. *Faraday Discuss.* **178**, 185–193 (2015).

30. BBI Solutions. Diagnostic Gold Colloid. https://www.bbisolutions.com/en/diagnostic-gc-starter-pack-plus.html.

31. Ge, A. *et al.* Interfacial Structure and Electric Field Probed by *in situ* Electrochemical Vibrational Stark Effect Spectroscopy and Computational Modeling. *J. Phys. Chem. C* **121**, 18674–18682 (2017).

32. Boxer, S. G. Stark Realities. *J. Phys. Chem. B* **113**, 2972–2983 (2009).

33. Nelson, D. A. & Schultz, Z. D. Influence of Optically Rectified Electric Fields on the Plasmonic Photocatalysis of 4-Nitrothiophenol and 4-Aminothiophenol to 4,4-Dimercaptoazobenzene. *J. Phys. Chem. C* **122**, 8581–8588 (2018).

34. Compton, R. G. & Banks, C. E. *Understanding Voltammetry*. (Imperial college press, 2010).

35. Akkerman, H. B. *et al.* Electron tunneling through alkanedithiol self-assembled monolayers in large-area molecular junctions. *Proc. Natl. Acad. Sci.* **104**, 11161–11166 (2007).

36. Poon, J. *et al.* Altered Electrochemistry at Graphene- or Alumina-Modified Electrodes: Catalysis vs Electrocatalysis in Multistep Electrode Processes. *J. Phys. Chem. C* **119**, 13777–

426   13784 (2015).

427   37.   Hu, Y. *et al.* Tracking Mechanistic Pathway of Photocatalytic CO2 Reaction at Ni Sites Using
428   Operando, Time-Resolved Spectroscopy. *J. Am. Chem. Soc.* **142**, 5618–5626 (2020).

429   38.   Farkas, E., Enyedy, É. A., Micera, G. & Garribba, E. Coordination modes of hydroxamic acids
430   in copper(II), nickel(II) and zinc(II) mixed-ligand complexes in aqueous solution. *Polyhedron*
431   **19**, 1727–1736 (2000).

432   39.   Readman, C. *et al.* Anomalously Large Spectral Shifts near the Quantum Tunnelling Limit in
433   Plasmonic Rulers with Subatomic Resolution. *Nano Lett.* **19**, 2051–2058 (2019).

434   40.   Liu, Y. C., Hwang, B. J. & Jian, W. J. Effect of preparation conditions for roughening gold
435   substrate by oxidation-reduction cycle on the surface-enhanced Raman spectroscopy of
436   polypyrrole. *Mater. Chem. Phys.* **73**, 129–134 (2002).

437   41.   Carnegie, C. *et al.* Room-Temperature Optical Picocavities below 1 nm3 Accessing Single-
438   Atom Geometries. *J. Phys. Chem. Lett.* **9**, 7146–7151 (2018).

439   42.   Anderer, C., Näther, C. & Bensch, W. Bis(2,2':6',2''-terpyridine-K^3 N,N' ,N'')nickel(II)
440   bis(perchlorate) hemihydrate. *IUCrData* **1**, x161009 (2016).

441   43.   Becke, A. D. Density-functional thermochemistry. III. The role of exact exchange. *J. Chem.*
442   *Phys.* **98**, 5648–5652 (1993).

443   44.   Frisch, M. J. *et al.* Gaussian 09 Revision E. (2009).

444   45.   Grimme, S., Ehrlich, S. & Goerigk, L. Effect of the Damping Function in Dispersion
445   Corrected Density Functional Theory. *J. Comput. Chem.* **32**, 1456–1465 (2011).

446   46.   Foster, J. P. & Weinhold, F. Natural hybrid orbitals. *J. Am. Chem. Soc.* **102**, 7211–7218
447   (1980).

448   47.   Reed, A. E., Curtiss, L. A. & Weinhold, F. Intermolecular interactions from a natural bond
449   orbital, donor-acceptor viewpoint. *Chem. Rev.* **88**, 899–926 (1988).

450   48.   Weigend, F. & Ahlrichs, R. Balanced basis sets of split valence, triple zeta valence and
451   quadruple zeta valence quality for H to Rn: Design and assessment of accuracy. *Phys. Chem.*
452   *Chem. Phys.* **7**, 3297–3305 (2005).

453   49.   Marenich, A. V, Cramer, C. J. & Truhlar, D. G. Universal Solvation Model Based on Solute
454   Electron Density and on a Continuum Model of the Solvent Defined by the Bulk Dielectric
455   Constant and Atomic Surface Tensions. *J. Phys. Chem. B* **113**, 6378–6396 (2009).

456   50.   Tissandier, M. D. *et al.* The proton's absolute aqueous enthalpy and Gibbs free energy of
457   solvation from cluster-ion solvation data. *J. Phys. Chem. A* **102**, 7787–7794 (1998).

458
459

Author contributions

D.W., Q.L., E.Reisner and J.J.B. conceived the research and developed the experiments. D.B., T.F. and E.Rosta carried out density functional theory calculations and provided input on catalytic interpretation. A.W. and E.Reisner provided input on interpretation of electrochemical and catalytic results. J.G. helped with spectral analysis. C.R. helped with synthesis of **Ni(tpyS)$_2$** D.W., Q.L., D.B., T.F. and J.J.B. analysed the data and wrote the manuscript with input from all authors.

Competing interests

The authors declare no competing interests.

Additional information

Supplementary information is available for the following files: UV-Vis spectra, dark-field image, additional cyclic voltammograms, dark-field scattering spectra, SERS spectra, and DFT calculations in pdf file; and the atomic coordinates of the optimised models are provided in Supplementary Data 1.